Numerical simulations of granular shear zones using the distinct element method
1. Shear zone kinematics and the micromechanics of localization

Julia K. Morgan

Department of Geology and Geophysics, SOEST, University of Hawaii at Manoa, Honolulu

Margaret S. Boettcher

Department of Geological Sciences, Brown University, Providence, Rhode Island

Abstract. Two-dimensional numerical simulations were conducted using the distinct element method (DEM) to examine the influences of particle size distribution (PSD) and interparticle friction μ_p on the nature of deformation in granular fault gouge. Particle fracture was not allowed in this implementation but points in PSD space were examined by constructing assemblages of particles with self-similar size distributions defined by the two-dimensional power law exponent D. For these numerical "experiments," D ranged from 0.81 to 2.60, where $D = 1.60$ represents the two-dimensional equivalent of a characteristic PSD to which cataclastically deforming gouge is thought to evolve. Experiments presented here used μ_p values of 0.10 and 0.50 and were conducted using normal stress σ_n on the shear zone walls of 70 MPa. Shear strain within these simulated assemblages was accommodated by intermittent displacement along discrete slip surfaces, alternating between broadly distributed deformation along multiple slip planes and highly localized deformation along a single, sharply defined, subhorizontal zone of slip. Slip planes corresponded in orientation and sense of shear to shear structures observed in natural gouge zones, specifically Riedel and Y shears; the oblique Riedel shears showed more extreme orientations than typical, but their geometries were consistent with those predicted for low-strength Coulomb materials. The character of deformation in the shear zone varied with PSD due to changes in the relative importance of interparticle slip and rolling as deformation mechanisms. A high degree of frictional coupling between large rolling particles in low D (coarse-grained) assemblages resulted in wide zones of slip and broadly distributed deformation. In higher D assemblages ($D >= 1.60$), small rolling particles self-organized into columns that separated large rolling particles, causing a reduction in frictional resistance within the deforming assemblage. This unusual particle configuration appears to depend on a critical abundance of small particles achieved at $D \approx 1.60$ and may enable strain localization in both real and simulated granular assemblages.

1. Introduction

Well-developed brittle shear zones are often characterized by significant accumulations of fault gouge or breccia, consisting of disaggregated and comminuted country rock and its diagenetic products. The presence of these particulate materials plays an inportant role in defining the structural character and mechanical behavior of the fault zone during sliding [e.g., *Scholz*, 1990]. Field exposures of gouge-filled fault zones reveal that much of the strain occurs within the gouge itself, generating characteristic fabrics and microstructural arrays that are thought to correlate with strain history and intensity and may yield insight into the seismic behavior of natural fault zones [e.g., *Chester and Logan,*

1989]. Numerous laboratory experiments have been conducted on simulated gouge (e.g., granular quartz, calcite, or powdered granite) to define controls on the formation of gouge structures and their correlations with fault strength and sliding behavior [e.g., *Logan et al.,* 1979, 1992; *Dieterich,* 1981; *Biegel et al.,* 1989; *Morrow and Byerlee,* 1989; *Marone et al.,* 1990; *Gu and Wong,* 1994; *Beeler et al.,* 1996]. Despite the wealth of data coming out of these experiments, there are still many unanswered questions, in particular, regarding how fault zones evolve, and what micromechanical phenomena drive their deformation behavior.

One of the more fundamental observations relating to fault rocks is that they experience changes in grain size, particle size distribution (PSD, representing the relative abundances of particle sizes), and mineralogy, over time. The gouge zone progressively widens with shear strain [*Robertson,* 1982; *Scholz,* 1987], as damaged wall rocks are incorporated into the fault zone and undergo progressive breakage and grain size reduction during cataclastic flow [*Scholz,* 1990]. Grain

distribution is thought to evolve through cataclasis toward a characteristic, self-similar PSD with a three-dimensional power law exponent, D_{3D} of about 2.60 [*Sammis et al.*, 1986, 1987; *Sammis and Biegel*, 1989; *Blenkinsop*, 1991]. This value may define a PSD in which grain fracture is minimized and interparticle sliding is enhanced, thereby influencing the deformation character, and probably the sliding behavior, of the gouge [*Biegel et al.*, 1989; *Marone and Scholz*, 1989; *Sammis and Steacy*, 1994].

The types of microstructures that form during shear, and the mechanical properties of the gouge, do appear to be strongly influenced by particle size and PSD [e.g., *Dieterich*, 1981; *Gu and Wong*, 1994; *Biegel et al.*, 1989; *Marone and Scholz*, 1989; *Logan et al.*, 1992], but the controls on the behaviors and fabrics that develop during deformation are incompletely understood. However, we can use numerical simulations of the discrete mechanics of the granular system, for example using the distinct element method (DEM) developed by *Cundall and Strack* [1979], to look inside shear zones as they deform and evolve. The utility of this approach was demonstrated earlier by *Antonellini and Pollard* [1995], who performed small strain simulations to study the generation and growth of shear bands; they briefly explored the influence of PSD on peak strength and failure behavior of granular assemblages. In this paper, and in the companion paper by *Morgan* [this issue], we present a series of higher shear strain DEM experiments of simulated gouge-filled shear zones to document more completely how PSD variations influence deformation and mechanical behavior of shear zones. This discrete numerical approach captures the discontinuous nature of microstructure formation, propagation, and dissipatation, thereby shedding light on transient deformational processes in gouge zones.

In this implementation of the DEM, particle fracture is not allowed; we do not attempt to simulate the exact process of real gouge undergoing progressive comminution but rather to sample points in PSD space; the snapshots of particle configurations and deformational processes may then be recombined to infer gouge evolution. In this way, we hope to isolate mechanisms that are active under a given set of conditions and observe how these change with strain. We also do not simulate the velocity dependence of sliding friction here, which might influence sliding stability [e.g., *Marone et al.*, 1990; *Beeler et al.*, 1996; *Nasuno et al.*, 1997]. In this paper we focus on the character of deformation in the simulated assemblages, specifically, related to interparticle deformation mechanisms, localization tendencies, and geometries of microstructures. The effects of PSD and mineralogy on mechanical strength and behavior are addressed by *Morgan* [this issue].

2. Distinct Element Method

The distinct element method (DEM) [*Cundall and Strack*, 1979; *Cundall and Hart*, 1989] is derived from molecular dynamics and simulates the dynamics of discrete particles which interact according to fundamental laws of contact physics. This technique has been successfully used to approximate the behavior of noncohesive, granular systems (for example, composed of sand or uniform spheres) under low stress conditions. Comparisons of DEM simulations and analogous laboratory experiments demonstrate qualitatively similar behaviors [*Cundall et al.*, 1982; *Thornton and Barnes*, 1986; *Cundall*, 1988]. Like natural granular materials [e.g.,

Wood, 1990; *Feda*, 1982], DEM systems can be induced to deform by ductile, intergranular flow [e.g., *Cundall*, 1988] or by the formation of discrete shear bands [e.g., *Scott*, 1996], depending on boundary conditions and stress history. True intragranular fracture that may accompany granular deformation, particularly at high stresses, has proven to be more difficult to capture using DEM techniques [e.g., *Antonellini and Pollard*, 1995; *Malan and Napier*, 1995; *Sadd and Gao*, 1997]; The favored approach is to construct granular aggregates that can break down under stress [e.g., *Bruno and Nelson*, 1991; *Trent and Margolin*, 1994, 1995] . However, in this study, which represents a first exploration of the method, we have neglected this mechanism. The full details of the DEM method are presented in the appendix.

3. Design of Numerical Experiments

The main objective of our DEM experiments was to explore the behavior of noncohesive granular materials within a simulated shear zone in order to study the effects of certain variables, in particular, PSD defined by the two-dimensional power law exponent D, interparticle friction μ_p, and normal stress σ_n. To isolate the influences of these factors, as many other variables as possible were held constant: physical constants such as particle sizes, elastic constants of the particles, density, and strain rate; experimental and numerical variables such as initial dimensions of the shear zone, total shear strain, and time step, etc. Experimental values are tabulated in Table 1. Each experiment was taken to 200% strain, in order to reach residual strength and deformation conditions. Overall, more than 100 DEM experiments were run; in this study we focus on only six experiments conducted for three D values: 0.81 (similar to coarse-grained, fractured breccia, or gouge), 1.60, and 2.60 (fine-grained, matrix-dominated gouge), μ_p of 0.50 and 0.10, and σ_n of 70 MPa.

The initial particle assemblage was created by randomly generating a specified number of spheres of four different sizes: 500, 250, 125, and 62.5 μm, within a two-dimensional domain. Relative particle abundances were determined according to the following power law relationship [e.g., *Sammis et al.*, 1986, 1987]:

Table 1. Physical and Numerical Parameters for Shear Zone Experiments

Parameter	Value
physical constants	
particle sizes (radius)	500, 250, 125, 62.5 μm
particle density*	1 kg/m^3
shear modulus	29 GPa
Poisson's ratio	0.20
experimental variables	
shear zone thickness (initial)	0.90 mm
shear strain rate (approximate)	1.11 x 10^{-6}
total shear strain	200%
numerical variable	
time step*	2.2613 s

* Particle density only factors into determination of the numerical time step, so if the system is stable, the density need not be realistic.
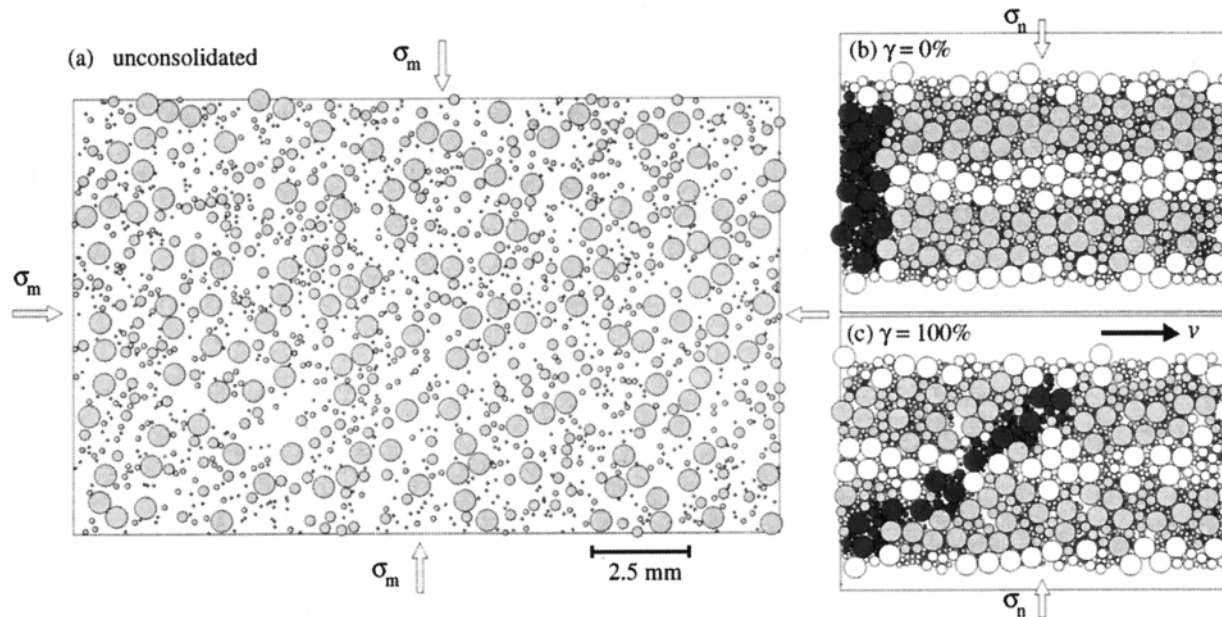
Figure 1. Experimental design. (a) Particles of four sizes were randomly generated within the domain with periodic boundaries. Domain boundaries were moved inward until the chosen consolidation mean stress σ_m was attained. (b) The lateral dimension was fixed at L, a constant normal stress σ_n was set to σ_m, and rows of particles in the consolidated volume were fixed relative to each other to define shear zone walls (white particles at top and bottom) spaced $W = 0.9$ mm apart. Shaded particles within the domain represent vertical (dark) and horizontal (light) strain markers. (c) A constant lateral velocity was assigned to the top wall to impose shear conditions on the assemblage.

$$N_i = N_{max} *(R_{max}/R_i)^D, \qquad (1)$$

where R_{max} and R_i and N_{max} and N_i represent the maximum and incremental particle sizes and abundances, respectively, and D represents the two-dimensional power law exponent, which differs from the three-dimensional value referred to earlier. (Note that *Turcotte* [1986] has shown that the two quantities are related, such that $D = D_{3D} - 1$.) The largest particles were generated first, and the smaller ones squeezed into the remaining space with no overlap (Figure 1a). In order to capture true three-dimensional contact mechanics [*Johnson*, 1985], spherical particles centered on the x-y plane were used in these two-dimensional simulations, rather than the more common cylinders or disks [e.g., *Antonellini and Pollard*, 1995]; particle displacements and rotations were constrained to that plane.

The volume was then consolidated by moving the x and y boundaries of the domain inward, until the desired isotropic mean stress was attained. Periodic x and y boundaries were used during consolidation, so particles near the boundaries of the volume interacted with images of particles found near the opposite boundary; particles that exited through one wall, reentered the domain through the opposite one. In this way, the number of particles remained constant and boundary effects were reduced [e.g., *Allen and Tildesley*, 1987].

Once the predetermined mean consolidation stress was reached, the shear zone was configured for the experiment. The lateral boundaries of the domain were fixed at a distance L, and two rows of particles within the consolidated volume were fixed relative to eachother to represent the shear zone walls (Figure 1b). The walls preserved the PSD of the assemblage and contained asperities which protruded into the shear zone;

this ensuring coupling of wall displacements with the gouge zone and precluding slip along the boundaries. Walls were initially spaced at $W_0 = 0.90$ cm apart. Shaded particles define strain markers in the gouge: a vertical column of dark particles along the left boundary; a horizontal row of lightly shaded particles at the center of the zone. Shear deformation was induced by moving the upper wall to the right at a constant velocity v. The bottom wall was held fixed (Figure 1c). Vertical displacements of the walls were allowed to maintain constant normal stress σ_n on the walls equal to the consolidation stress. Shear strain was calculated as $\gamma = dx_1/W$, where x_1 is the horizontal dimension and W is the instantaneous thickness of the shear zone.

Data on shear zone configurations, particle positions, displacements, rotations, and interparticle contact forces were stored throughout each experiment at 2% strain increments to map out deformation within the shear zone. Bulk properties of the shear zone, for example, porosity, volumetric stresses, contact number, and average interparticle contact force, were collected more frequently, allowing the evolution of various physical and mechanical properties to be tracked throughout the experiment. Discussion of these data is reserved for the paper by *Morgan* [this issue].

4. Visualizing Shear Zone Deformation

Granular deformation can be studied by comparing sequential snapshots of shear zone configuration. Over small strain increments, however, it is difficult to detect relative particle motions which would elucidate the distribution, persistence, and micromechanics of deformation. In order to better illustrate shear zone deformation, we plotted particle
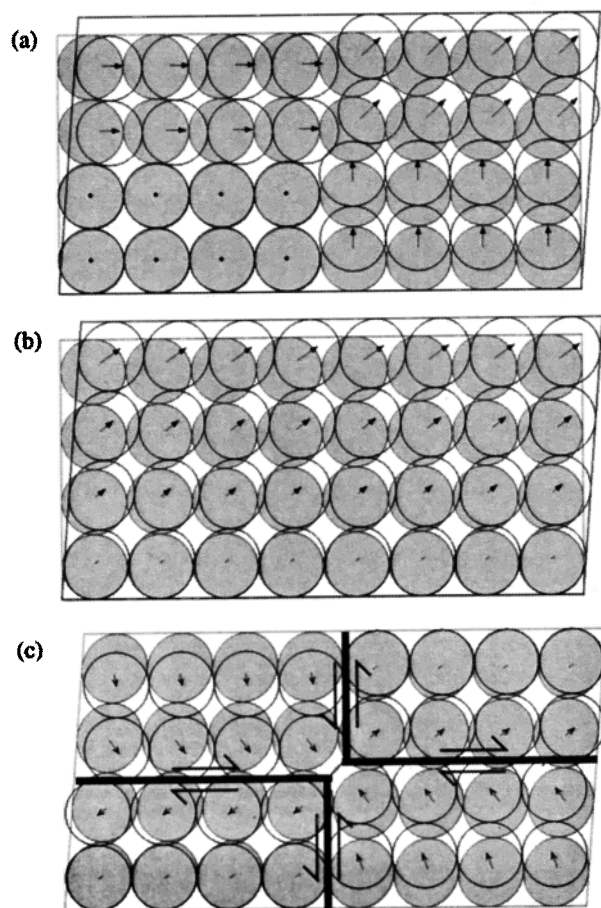
(a)

(b)

(c)

Figure 2. Schematic diagram describing deformation plots. (a) Particle displacements over an increment of strain are shown by arrows connecting particle centers of initial (shaded) and final (outlined in black) particle configurations. (b) Displacements resulting from corresponding homogeneous strain of the domain and particles (outlined in black). (c) Residual displacements (arrows) are differences between particle displacements (outlined in black), and displacements due to homogeneous strain (shaded). The directional derivative given by equation (2) highlights the discontinuities in the deformation field, i.e., zones of slip (solid lines), and their sense of shear.

rotations and gradients of residual displacements, that is, differences between particle displacements (Figure 2a) and displacements due to homogeneous shear strain (Figure 2b) [*Williams and Rege,* 1996] over a given strain increment. Small residual displacements throughout the shear zone define a distributed, nearly homogeneous strain field, while large residual displacements indicate significant heterogeneity (Figure 2c). This emphasizes heterogeneities in the strain field, rather than the magnitudes of displacements.

The gridding, gradient calculation, and display capabilities of GMT software [*Wessel and Smith,* 1995] were then used to map the displacements. Incremental residual vector components were fit to a continuous curvature surface. A nearest-neighbor gridding algorithm was used to obtain spatially averaged residual displacement vectors, weighted by the inverse distance between the node and the particle of interest. Residual vectors pointing to the right (Figure 2c)

correspond to domains that have moved farther than predicted by the homogeneous displacement field (Figure 2b) and are apparently coupled to the upper plate; similarly, vectors pointing to the left represent domains that have moved less distance and are apparently coupled to the lower plate. A sharp discontinuity in vector directions and magnitudes indicates a slip plane within the shear zone (Figure 2c). In order to highlight the structural discontinuities we took the directional derivative of the horizontal displacement surface represented by z [*Wessel and Smith,* 1995]

$$Dz = -\left[\frac{dz}{dx_1}*sin(\alpha)+\frac{dz}{dx_2}*cos(\alpha)\right], \qquad (2)$$

where α is the counterclockwise angle from horizontal. This provides a map of the instantaneous shear zone structure incurred over the strain interval. Sharp discontinuities (slip planes) result in high positive or negative derivatives.

5. Results

5.1. Comparative Deformation Sequences for the PSD Assemblages

Variations in D result in distinct contrasts in appearance and deformation behavior of the granular assemblages, although shear zone thicknesses and particle sizes are identical. Sequences of images are shown for the first 10% strain for three experiments with μ_p = 0.50: F65, D = 0.81 (Plate 1), F30, D = 1.60 (Plate 2), and F33, D = 2.60 (Plate 3); higher and lower μ_p experiments prove to be qualitatively similar, so the differences will only be noted as needed. The sequences of images in Plates 1-3 correspond to phases of initial loading, reorganization of particles under shear stress, and the subsequent failure (sudden drop in stress, accompanied by localized slip) of these assemblages. Peak stress was reached by about 10% shear strain [*Morgan,* this issue]. Each PSD assemblage will be discussed independently.

5.1.1. F65, D = 0.81. The small number of particles and relative abundance of large particles imparts a very heterogeneous appearance to the D = 0.81 assemblage (Plate 1a). Interparticle contacts are dominated by large particle pairs, leaving large pore spaces between them. Although difficult to see over the small (2%) strain increments shown here, deformation was very jerky, as frictional particles interlocked, stresses built up, pore spaces expanded and the shear zone dilated; failure subsequently occurred by sudden slip along a plane of particles and the shear zone contracted. Changes in associated shear zone properties (e.g., stress and dilation) with strain are discussed more completely by *Morgan* [this issue].

The progression of microstructures during the initial loading phase can be seen in Plate 1b. At 2% strain, the broad distribution of anastomosing, subhorizontal slip planes accommodating synthetic displacement (i.e., consistent with the sense of shear; red bands) reveals generally distributed deformation within the shear zone. By 8% strain, slip had focused into two discrete synthetic slip zones near the top and base of the shear zone, and by 10% strain, slip had localized onto a single, synthetic plane near the base of the shear zone.

The distribution of particle rotations shows a direct correlation with the positions of the slip planes (Plate 1c). The slip planes identified in Plate 1b consist of relatively broad zones of rolling particles, dominated by large particles.
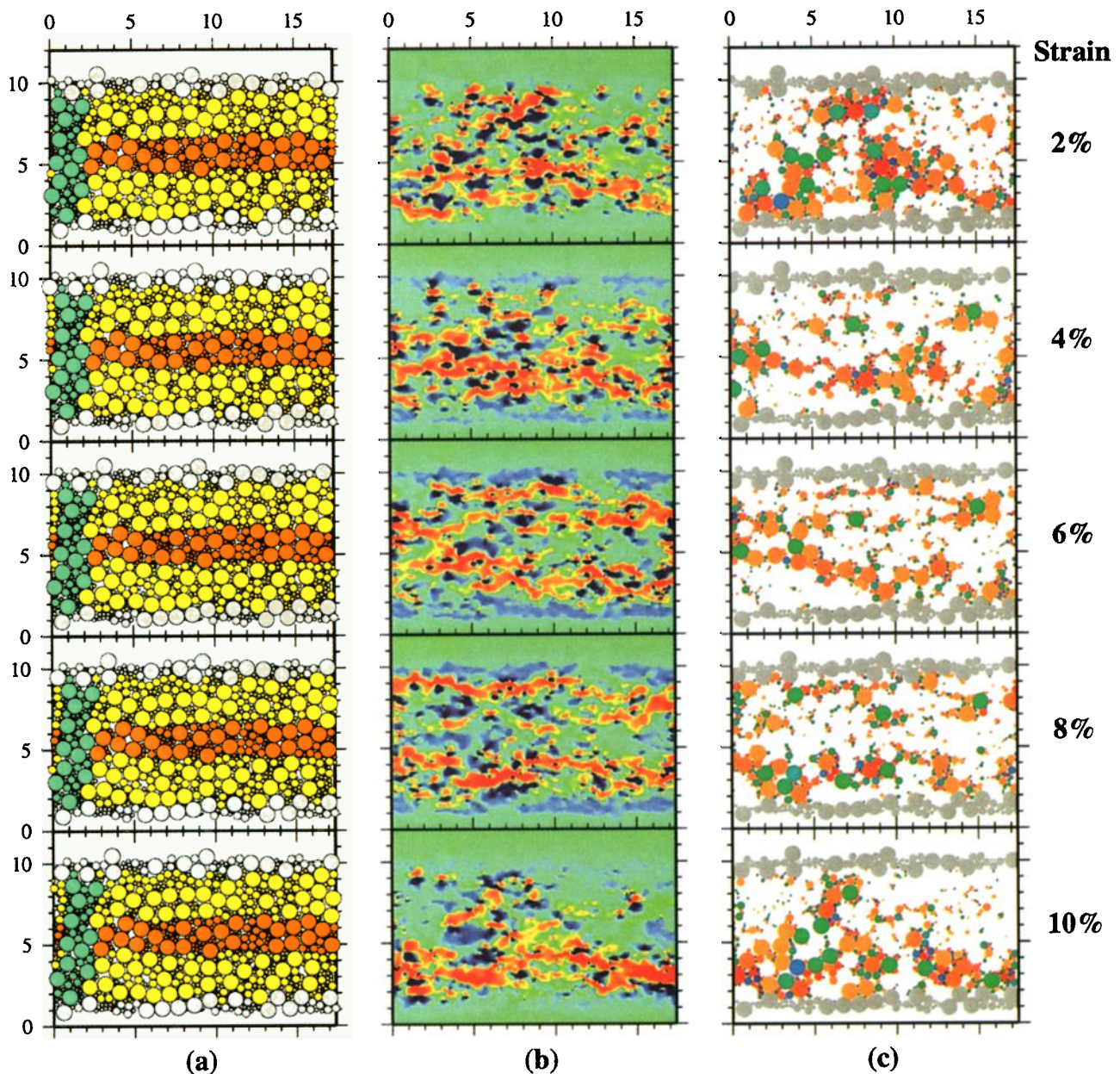
Plate 1. Experiment F65, $D = 0.81$, $\mu_p = 0.50$, $\sigma_n = 70$ MPa, 2-10% strain. (a) Particle configurations; gray particles denote walls; green and orange particles define vertical and horizontal strain markers, respectively. (b) Directional derivative of the horizontal component of the residual displacements, calculated using equation (2); transitions in color from yellow, orange, to red denote increasing synthetic shear on the slip planes (in a direction consistent with displacement on the shear zone); transitions through light blue, dark blue, and violet denote increasing antithetic shear (in a direction opposite to the displacement on shear zone). (c) Incremental particle rotations; white indicates no rotation; transitions through yellow, orange, and red denote increasing synthetic rotation; transitions through light green, dark green, and blue denote antithetic rotation.

Most of the particles rotated in a synthetic direction, but particles rotating in the antithetic direction (opposite to the sense of shear) were dispersed throughout the domain. This is a fundamental characteristic of low D systems that contain many large particles in contact. The large particles are frictionally coupled and interlocked, such that synthetic rotation of one induces antithetic rotation in another. This distributes the disturbance to adjacent regions, leading to relatively wide, diffuse zones of slip. Both lower and higher

μ_p assemblages showed very similar distributions of rolling particles, but the magnitude of rotation increased with μ_p.

5.1.2. F30, $D = 1.60$. At $D = 1.60$ the assemblage contains more particles and proportionally more small particles, which begin to define a fine-grained matrix (Plate 2a). Interparticle contacts are distributed among large and small particle pairs; large pore spaces are still occasionally present, but the assemblage is apparently more tightly packed. Deformation proceeded somewhat more smoothly
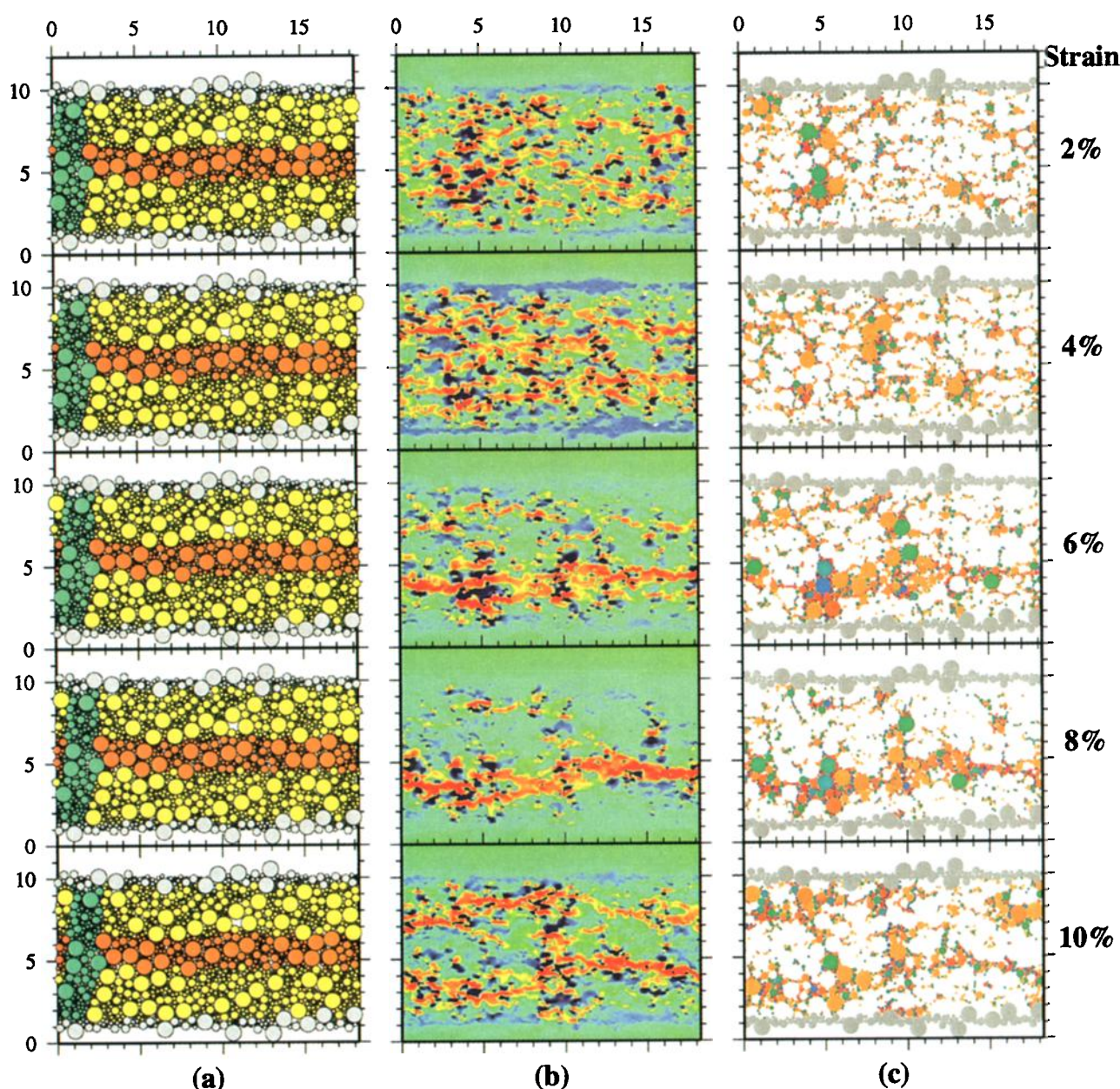
Plate 2. Experiment F30, D = 1.60, μ_p= 0.50, σ_n= 70 MPa, 2 - 10% strain. Same as in Plate 1.

than in the low D assemblage, as smaller particles filled the pore spaces and variations in dilation were reduced.

The displacement gradient plot sequence (Plate 2b) again reveals that deformation progressed from relatively distributed slip on many anastamosing, synthetic subhorizontal slip planes at 2% strain to localized slip on a single slip plane near the base of shear zone plot by 8% strain. A second slip plane was intermittently active near the top of the shear zone at both 6% and 10% strain. At times, synthetic slip planes developed at an angle to the shear zone, especially at 6% and 10% strain, but in this sequence they were short-lived. A second set of deformation structures is evident in these images at high angles to the shear zone walls (diffuse, blue-violet features). The subvertical slip planes reflect an antithetic sense of shear and were best developed when deformation was distributed across the shear zone, e.g., 2-4% strain. By 6-10% strain, the

subvertical slip planes had narrowed to become subtle subvertical disturbances adjacent to the well-developed low-angle slip planes.

The distribution of rolling particles shown in Plate 2c again shows direct correlation with deformation structures and a high degree of particle self-organization. The low-angle slip planes were dominated by synthetically rolling particles, both large and small, while high-angle planes were dominated by small antithetically rolling particles. The distribution of rotations is consistent with the sense of shear indicated in the displacement gradient plots. An interesting feature in these plots is the tendency for large particles, particularly in the low-angle slip zones, to show synthetic rotations, while smaller particles within the slip zones are guided into subvertical columns at the margins of the larger particles and show antithetic rotation. The columns extend into the
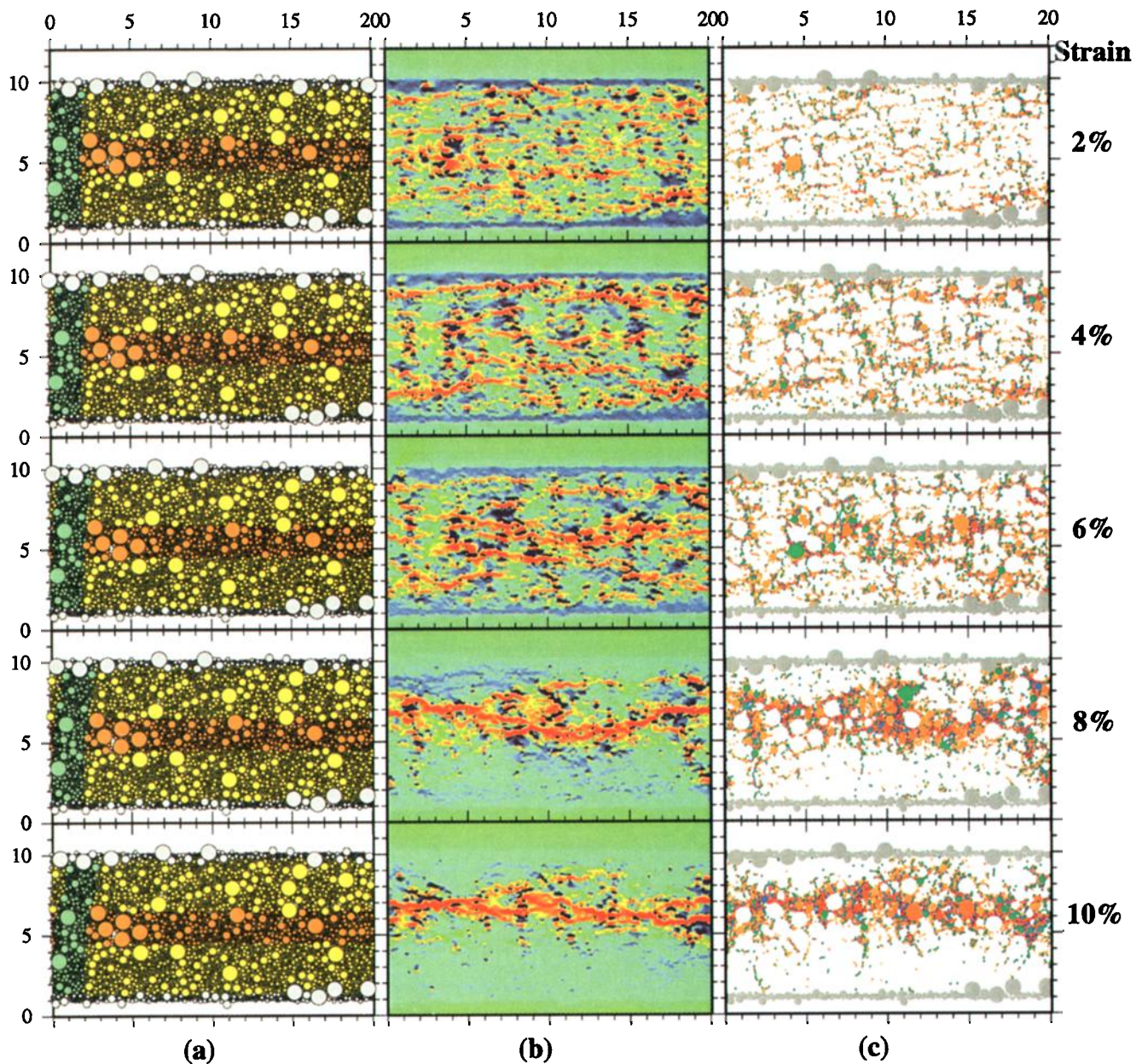
Plate 3. Experiment F33, D = 2.60, μ_p= 0.50, σ_n= 70 MPa, 2 - 10% strain. Same as in Plate 1.

surrounding volume, coinciding with high-angle, antithetic slip planes identified on both the displacement gradient and particle rotation plots. Again, particle rotation distributions were similar for all values of μ_p, but mean particle rotations increased with increasing μ_p.

5.1.3. F33, D = 2.60. For the high D assemblages, small particles dominate the system, composing a very fine-grained matrix that effectively isolates the larger particles and prevents their mutual contact (Plate 3a). In this assemblage the small particles played a very critical role in defining the nature of deformation. Pore spaces are not very evident, and the assemblage appears quite densely packed. Deformation was much smoother than in lower D simulations, and the fluctutations in stress and dilation were much smaller than in the lower D assemblages [*Morgan*, this issue].

As in the other assemblages, deformation was broadly distributed across multiple subhorizontal slip planes at 2% strain and progressively localized onto a single plane by 8-10% strain (Plate 3b). Individual slip planes, even at 2% strain, were very sharply defined, comprising single rows of small particles and involving large particles in a significant way only when slip became highly localized by 6% strain (Plate 3c). The small particles did most of the work, clearly rolling around larger static particles (white) within the zones of deformation. At low strains (γ < 6%), low-angle planes were typically oriented 5°-10° from horizontal and were progressively replaced by subhorizontal planes as strain localized from 6 to 10% strain. As with the D = 1.60 assemblages, subvertical columns of antithetically rolling particles are quite evident (green-blue bands) and best

developed when deformation was most broadly distributed (2-4% strain). The columns transect the low-angle planes, again often separating larger synthetically rolling particles. In general, the smallest particles accommodated the greatest rotations, especially within the zones of most concentrated slip at 8-10% strain. As for the other assemblages, the distribution of particle rotations was largely independent of μ_p, but the magnitude of rotation increases with μ_p.

5.2. Geometry and Persistence of Microstructures

The types of discrete microstructures observed in the deformation sequences in Plates 1-3 occurred throughout the experiments. As shown in Figure 3 for the two higher D simulations, these structures clustered around certain orientations, and can be classified accordingly (e.g., Figure 3a). The predominant and most long-lived features were subhorizontal Y shears, which can accommodate essentially infinite displacement. These occurred in all simulations and remained active for up to 15-20% strain. Multiple Y shears
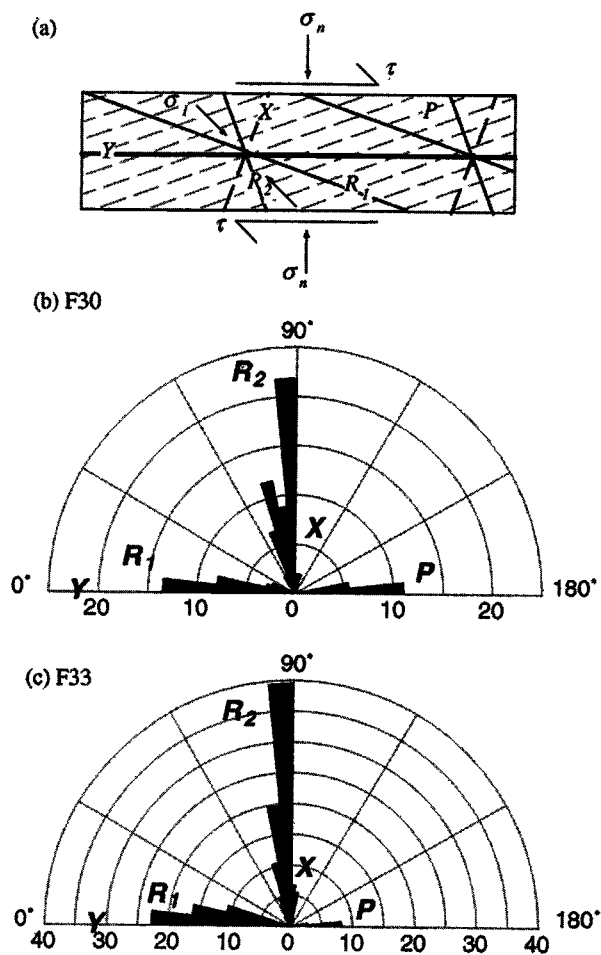

Figure 3. (a) Typical shear fracture array. Fault parallel Y shears accommodate large synthetic displacements. Oblique Riedel shears, R_1 and R_2, are symmetrically disposed about the principal stress orientation σ_1 and accommodate synthetic and antithetic shear, respectively. Antithetic X shears may develop in a direction complementary to R_2. Clay foliations or synthetic slip occur in low-angle P orientations, symmetrically oriented to R_1 [Logan et al., 1979]. (b) Slip plane orientations for test F30 ($D = 1.60$, $\mu_p = 0.50$), classified according to definitions in Figure 3a. (c) Slip plane orientations for test F33 ($D = 2.60$, $\mu_p = 0.50$).
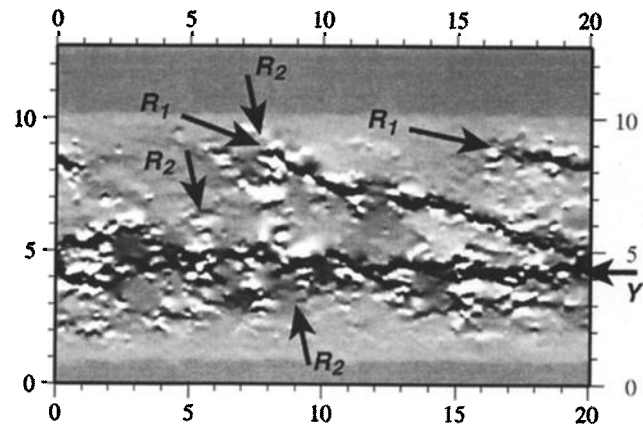

Figure 4. Example of coincident Y, R_1, and R_2 shears, revealed by plotting the directional derivative of residual displacements for F33 ($D = 2.60$, $\mu_p = 0.50$) at 140% strain. Synthetic sense of slip on the low-angle Y and R_1 shears is indicated by dark shades of gray; antithetic slip on the high-angle R_2 shears is shown by lighter shades. The R_1 shear in this example occurs at an unusually high angle of 15°, similar to that shown in Figure 3a.

might be active at one time, particularly in the higher D simulations (Plate 3) where smaller mean grain size provided many avenues for slip. Slip often alternated among several planes that remained active over several strain increments, but generally, the Y shears were eventually abandoned and slip transferred to another horizon.

Low-angle, oblique synthetic shears also occurred, most commonly in the two higher D simulations (e.g., Plate 2b, 10% strain; Plate 3b, 8% strain); these features showed similar orientations and senses of shear as low-angle Riedel (R_1) shears [e.g., Riedel, 1929; Mandl, 1988]. The R_1 shears typically developed at angles of 10°-15° to the shear zone for all PSD assemblages with $\mu_p = 0.50$; in $\mu_p = 0.10$ experiments, R_1 shears showed a range around 5-10°. Occasional, well-developed R_1 shears developed and propagated at higher angles, particularly in the higher D experiments (Figure 4), closer to the 15°-20° observed in many natural shear zones [Logan et al., 1979]. The oblique orientations of the R_1 shears introduced geometric constraints which limited the displacements they could accommodate, so they tended to be relatively short-lived, e.g., 10-12% strain. Commonly, with continuing strain, throughgoing Y shears crosscut and displaced the oblique shears (e.g., Plates 2 and 3).

The initial loading phases of the higher-D assemblages (2-4% strain, Plates 2 and 3) demonstrated other types of low-angle structures: P shears dipped 10°-15° away from the slip direction and accommodated displacement synthetic with the sense of shear (e.g., Figure 3). The P shears were incipient features defined by discontinuous rows of small particles, a single particle wide, that developed during the earliest stages of the simulation (0-8% strain). With strain, these shears widened and were apparently captured by adjacent shears, eventually propagating into a Y or R_1 shears (Plate 3c, 2-6% strain). Similar features were observed in the low μ_p experiments, but these lay at much lower, almost horizontal angles.

The subvertical antithetic shears are consistent with high-angle Riedel (R_2) or X shears [e.g., Riedel, 1929; Mandl, 1988], as shown in Figure 3. They were particularly abundant

in the higher D assemblages (Plate 3b), where they were defined by narrow columns of small particles but were more difficult to detect in the low D systems. They typically occurred at angles between 70° and 110° from horizontal for $\mu_p = 0.50$ experiments (Figures 3b and 3c), and between 75° and 100° for $\mu_p = 0.10$ experiments (not shown), with modes between 85° and 90° for both. Discrete, but very narrow, R_2 shears developed within the first 2% strain and persisted, widened, and lengthened until failure occurred at about 10% strain (Plate 3b). During the remainder of the experiment (not shown) they were not always as long-lived but tended to form and dissipate within 2-6% strain. In part, this was due to geometric constraints; their steep orientations prevent R_2 shears from accommodating significant offset. The R_2 shears were rarely observed to rotate; rather they dissipated and formed in more favorable orientations. From Figures 3b and 3c, high-angle shears appear more abundant than the low-angle shears. This reflects the fact that multiple R_2 shears were active over a single 2% strain increment during both distributed and localized deformation, but each accommodated very little offset, while a single, active low angle (R_1 or Y) shear experienced major displacement.

5.3. Stress Distributions and Failure Modes

Particle stresses will vary with the distribution of contacts and forces (equation (A12)) and should be related to shear zone kinematics and microstructure. Representative distributions of average differential stress on individual particles are shown in Figure 5 for three $\mu_p=0.50$ configurations. (Systems with $\mu_p=0.10$ are qualitatively similar, but the particles show slightly lower stress magnitudes.) The smallest particles carried the highest differential stress due to the anisotropy in contact distribution at the smallest scale. In the low D system (Figure 5a), large particles displayed a range of differential stresses and were organized into inclined columns of highly stressed particles reminiscent of the grain bridges inferred by *Sammis et al.* [1987]. The grain bridges bore much of the load from the shear zone walls and migrated through the shear zone with continuing strain. At intermediate D (Figure 5b), large particles showed a range of differential stress intensities, but grain bridges were not as well defined as in the low D system. Instead, smaller particles carried more of the load, defining inclined, highly stressed columns. At high D (Figure 5c), large particles bore very low differential stresses and appeared to float in the finer-grained matrix. Smaller particles organized into short, discontinuous bands under high stresses that distributed the load throughout the volume.

The orientations of maximum principal stress, σ_1 can be determined using equation (A13). The isotropic consolidation state at the start of the simulation resulted in relatively random distribution of σ_1 orientations for all assemblages. By the first 10% strain, σ_1 orientations have rotated to about 45° to the shear zone boundaries (Figure 5), consistent with experimental observations [e.g., *Mandl et al.*, 1977; Mandl, 1988]. In the low D assemblage, stress orientations were very heterogeneous due to the coarse particle size and small number of particles over which they are averaged (Figure 5a). The σ_1 orientations became more orderly with increasing D and decreasing mean grain size (Figures 5b and 5c), but retained some heterogeneity due to random particle distributions. Principal stress orientations varied between 45° and 50° during an experiment, correlating with loading and failure events, as noted experimentally by others [*Gu and Wong*, 1994].
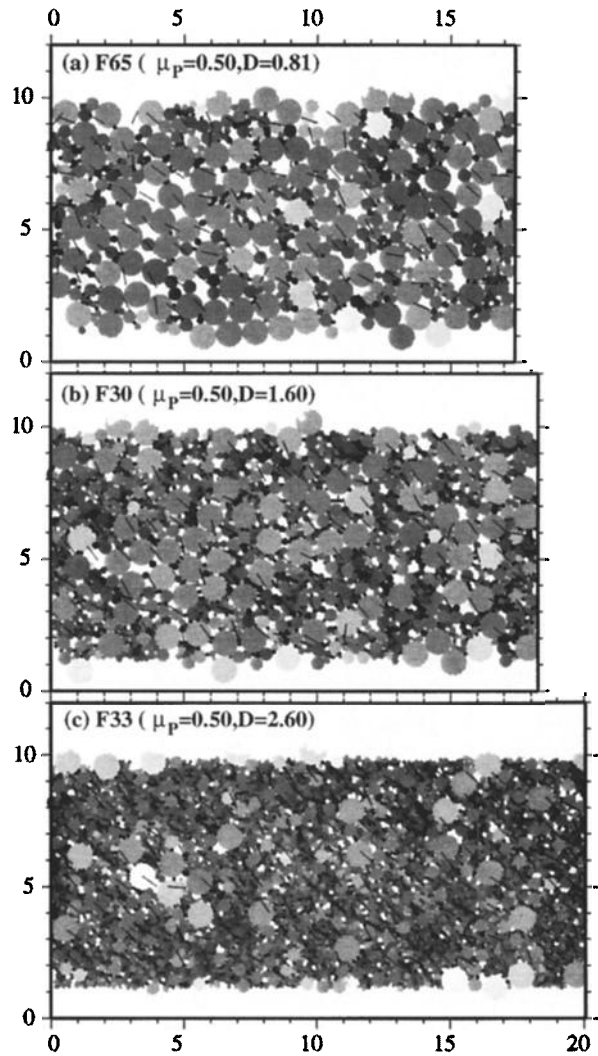

Figure 5. Instantaeous average differential particle stresses at 10% shear strain for for $\mu_p = 0.50$ experiments; white denotes no stress; increasing stress magnitudes are indicated by increasingly darker shades of gray. Maximum principal stress orientations σ_1 are indicated by black lines. (a) F65, $D = 0.81$; (b) F30, $D = 1.60$; (c) F33, $D = 2.60$.

The formation and failure of grain bridges related to the mode of granular deformation and the generation of localized slip planes in all assemblages, but these events occurred at different scales depending on the scale of the grain bridge. The process can be seen for the $D = 0.81$ system with $\mu_p = 0.50$ in Figure 6, where a sequence of images shows an inclined column of highly stressed particles which became progressively more diffuse and ultimately failed with continuing strain. Corresponding displacement gradient plots show a progression from broadly distributed deformation throughout the shear zone at 86% strain to more localized slip along a low-angle slip band following the failure of the grain bridge. This progression was accompanied by shear zone dilation as the load on the bridge increased and the grain bridge rotated to become more perpendicular to the shear zone walls; this was followed by shear zone contraction when the bridge failed and slip localized. As noted by *Cundall et al.* [1982], grain bridges failed by interparticle rolling between loaded particles; interparticle slip occurred primarily between
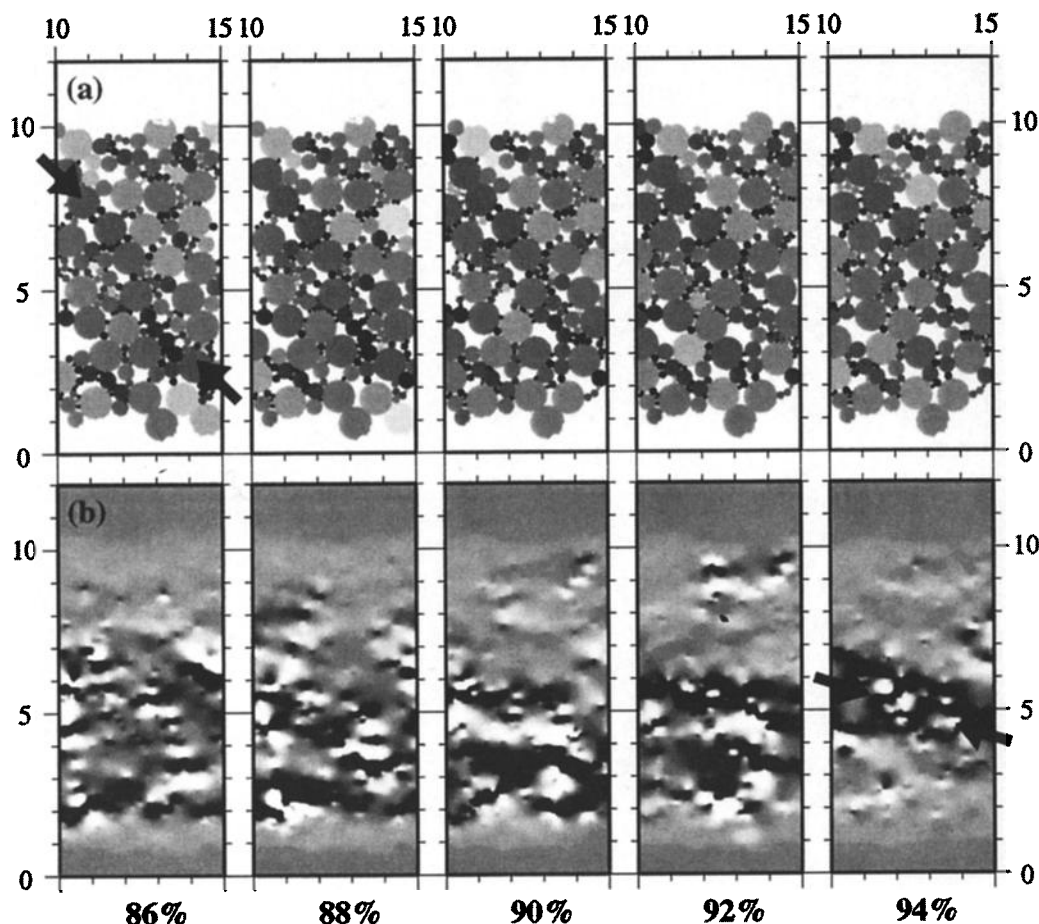
Figure 6. Failure of a stress bridge in test F65 ($D = 0.81$, $\mu_p = 0.50$). (a) Differential particle stress plots (shaded as in Figure 5) show an inclined column of large particles which bear relatively high differential stresses at 86% strain (arrows); particle stresses within the column decrease progressively through 94% strain, as indicated by lighter shades of gray. (b) The directional derivative of residual displacements (shaded as in Figure 4) reveals a transition from relatively distributed deformation, marked by multiple, low angle zones of slip (intermediate shades of gray) at 86% strain to relatively localized slip along a single plane (dark band) at 94% strain. The progressive localization of strain accompanies the failure of the stress bridge.

particles in the unloaded regions of the assemblage. The frequency of failures and the magnitudes of the resulting stress drops were influenced by the number of force-bearing contacts in the assemblage and the magnitudes of the contact forces. Thus the stress-strain behavior of high D simulations tended to be much smoother than that of low D assemblages [*Morgan*, this issue].

5.4. Cumulative Strain

The sequences of deformation displayed in Plates 1-3 show that strain accrued largely through discrete sliding events during which slip localized onto one or more planes. The final particle configurations (Figure 7) reveal that by 200% strain, deformation was relatively uniformly distributed throughout the domain. The originally vertical columns of shaded particles are rotated and elongated by the accumulated shear strain but maintain almost linear configurations. The horizontal bands of more lightly shaded particles remain centered within the shear zone but show some mixing with the surrounding particles. Overall, despite transient localizations of strain during the simulation, by the completion of the test

the finite strain was relatively uniformly distributed across the system. Exceptions occurred for some higher D experiments (e.g., Figures 3b and 3c), which experienced preferential shear near the upper boundary. This may result from statistical heterogeneity in grain size due to random particle generation or may be a reflection of the asymmetry of stress loading on the assemblage, as only the upper wall translated to induce shear strain.

6. Discussion

6.1. Deformation Mechanisms in Real and Simulated Gouges

The relevance of the simulation results presented here depends in large part on the validity of the deformation mechanisms operating within the assemblage and their similarity to real deformation mechanisms. A fundamental observation of lab experiments is that grain fracture plays a key role in the evolution of gouge during shear. This leads to the generation of spatial variations in grain size and PSD which relate to heterogeneities in stress and strain and may
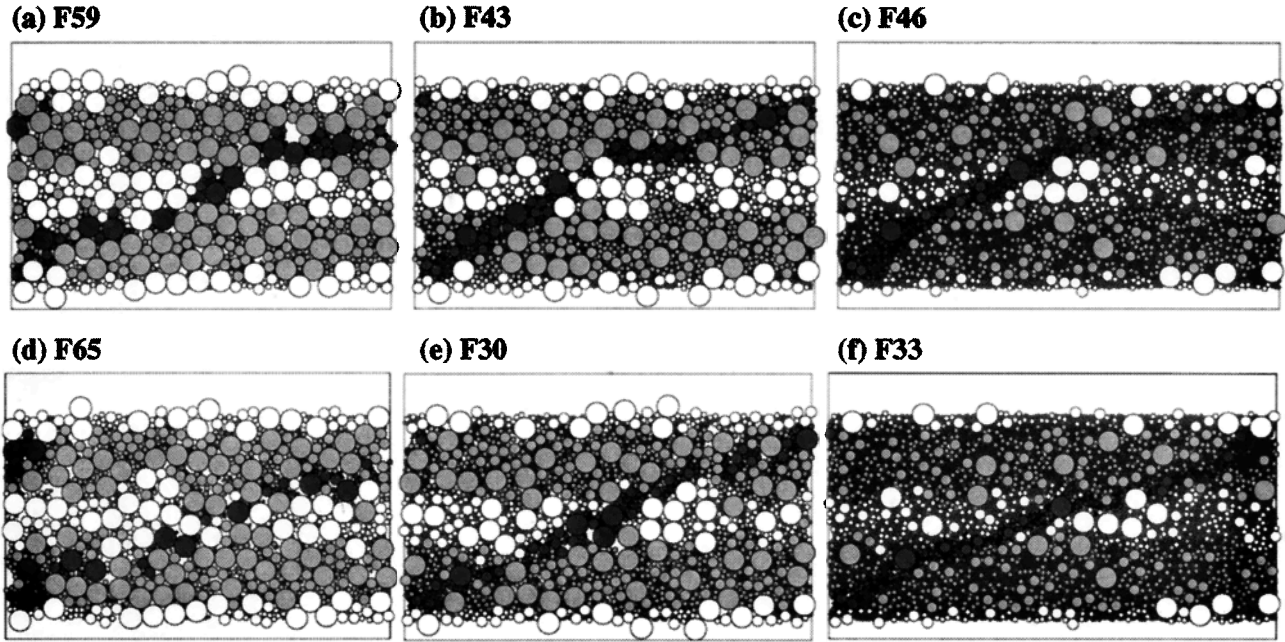
(a) F59 **(b) F43** **(c) F46**

(d) F65 **(e) F30** **(f) F33**

Figure 7. Cumulative deformation at 200% shear strain revealed by displacements of shaded strain markers. (a) F59, $D = 0.81$, $\mu_p = 0.10$. (b) F43, $D = 1.60$, $\mu_p = 0.10$. (c) F46, $D = 2.60$, $\mu_p = 0.10$. (d) F65, $D = 0.81$, $\mu_p = 0.50$. (e) F30, $D = 1.60$, $\mu_p = 0.50$. (f) F33, $D = 2.60$, $\mu_p = 0.50$.

tend to guide deformation into localized zones [e.g., *Marone and Scholz,* 1989; *Marone and Kilgore,* 1993; *Gu and Wong,* 1994]. Moreover, differential comminution of the gouge produces zones with reduced grain size which stand out, imparting an overall brittle appearance to the shear zone. The process of grain fracture itself will also influence the net strength of the assemblage [e.g., *Zhang et al.,* 1990; *Wong et al.,* 1997]. All of these influences are absent in our simulations due to the lack of grain fracture. Instead, our experiments serve to sample points in PSD space, from which we may infer the effects of variations in grain size and PSD on deformation mechanism and mode, and attempt to reconstruct the spatial and temporal evolution of a shear zone.

The use of spherical particles in the DEM simulations introduces another deformation mechanism that is commonly neglected in the context of granular gouge deformation [e.g., *Biegel et al.,* 1989], that of interparticle rolling. In fact, naturally deformed cataclastic rocks described by *Sammis et al.,* [1986, 1987], and simulated gouges produced in the laboratory [*Biegel et al.,* 1989; *Marone and Scholz,* 1989], are typically characterized by highly angular clasts which tend to resist interparticle rolling. However, field evidence suggests that particle rolling may become increasingly important as mean grain size decreases, and D increases; visible clasts within sheared gouges from brittle fault zones in Death Valley, California, all showed some degree of rounding [*Morgan et al.,* 1996; *Cladouhos,* 1998], and a direct correlation has been made between clast rounding and D value in fine-grained gouges [*Morgan et al.,* 1996] and deformed tills [*Hooke and Iverson,* 1995]. Particle rounding may result from an increased tendency toward interparticle sliding and abrasion with comminution and PSD evolution, perhaps as the abundance of smaller particles increases, and they begin to play a "lubricating" (and polishing) role within discrete shear zones. By this reasoning, the micromechanisms of

deformation simulated in these DEM experiments approach those of real fault rocks as D increases; interparticle rolling and sliding become increasingly important with increasing D, as intragranular fracture is inhibited by the isolation of large particles within the fine-grained matrix [e.g., *Sammis et al.,* 1987; *Biegel et al.,* 1989]. In the lower D simulations, interparticle rolling may serve as a proxy for grain fracture that occurs in real rocks, providing a mechanism to relieve stresses that build during frictional coupling between particles.

6.2. Geometry of Microstructures:

Naturally and experimentally deformed gouges commonly develop characteristic shear fracture arrays similar to those observed in our simulations [e.g., *Logan et al,* 1979, 1992; *Marone and Scholz,* 1989; *Marone et al.,* 1990; *Gu and Wong,* 1994; *Beeler et al.,* 1996]. Idealized orientations are shown in Figure 3; R_1 shears are commonly oriented ~15° from the shear plane, and high angle R_2 shears at about 68° [e.g., *Logan et al.,* 1979, 1992]. The microstructures revealed in our simulations typically formed at more extreme angles, nearly parallel (R_1 and P shears) and perpendicular (R_2 and X shears) to the shear plane (Plates 1-3 and Figure 3). We need to consider whether these orientations are consistent with predicted geometries given the nature of the deforming material.

By definition, Riedel shears are Coulomb structures that obey the Coulomb failure criterion [e.g., *Riedel,* 1929; *Mandl,* 1988]; they should be symmetrically disposed about the maximum principal stress σ_I, with angles relative to σ_I defined as

$$\theta = 45° - \phi_f/2, \qquad (3)$$

where $\mu_f = tan\,\phi_f$. This yields θ of 26° and ϕ_f of 37°

consistent with Byerlee's law for friction [*Byerlee*, 1978]. Shear zone strength, represented by average fault friction μ_f, will influence the orientations of shear structures [e.g., *Mandl*, 1988]. As discussed in more detail by *Morgan* [this issue], the residual coefficient of friction μ_f was quite low for all simulations, ranging from about 0.25 to 0.20 for low μ_p to high μ_p experiments, respectively. From equation (3), these values yield θ values of 37° and 39°, for low and high μ_p systems respectively. The orientations of σ_1 for all experiments lay between 45° and 50° from the shear plane, decreasing slightly with increasing D.

If the simulated gouge obeys equation (3), such high values for θ would lead to R_1 shears oriented 7°-11° in the low μ_p systems and 9°-13° in the high μ_p systems; R_2 shears would be oriented almost vertically, at about 85°-89° in the low μ_p systems and 83°-87° in the high μ_p systems. Synthetic P shears and antithetic X shears would develop at conjugate orientations symmetric to R_1 and R_2 shears respectively across the shear plane. These orientations are consistent with those observed in our simulations, suggesting that the simulated gouge can be described as a Coulomb material. Steeper R_1 shears, for example, those between 10° and 20°, may stand out in the simulations (Figure 4), because they can be easily distinguished from Y shears. The confusion between R_1 and Y shears is compounded by the numerical constraint of periodic lateral boundaries; features exiting one boundary reenter the opposite boundary, where they may be captured by parallel structures, or by the tail of the same structure (e.g., Plate 3b from 8% to 10% strain). This may preclude the preservation of true R_1 shears in these simulations. The range of orientations for R_2 shears (and X shears) is also consistent with predictions. The narrower range for R_2 shears in the low μ_p systems may reflect the slightly higher value for θ in the weaker material.

6.3. Structural and PSD Evolution of Fault Gouge

Laboratory experiments of gouge deformation demonstrate repeatable progressions of microstructures, which correlate well with mechanical strength and behavior [e.g., *Marone and Scholz*, 1989; *Morrow and Byerlee*, 1989; *Logan et al.*, 1992; *Gu and Wong*, 1994; *Beeler et al.*, 1996]. During the earliest phases of deformation, coarse-grained gouge experiences largely distributed deformation, associated with cataclasis and shear zone compaction; this may last up to 100% strain (several millimeters of displacement) and is often manifested by strain hardening. Particle comminution is thought to lead to a stable PSD [*Sammis et al.*, 1986, 1987] within which shear stresses are dissipated more efficiently by mechanisms other than whole grain fracture, for example, interparticle sliding [e.g., *Biegel et al.*, 1989], abrasion [*Hooke and Iverson*, 1995], or rolling [*Morgan et al.*, 1996]. In three dimensions, this characteristic PSD has been identified at $D_{3D} = 2.60$ [*Sammis et al.*, 1986, 1987; *Sammis and Biegel*, 1989], corresponding to two-dimensional $D = 1.60$ [*Turcotte*, 1986]. Others have suggested that this characteristic PSD may define an optimal configuration enabling strain localization [e.g., *Biegel et al.*, 1989; *Marone and Scholz*, 1989]. The occurrence of incipient Riedel shears at peak strength [*Logan et al.*, 1992] and possibly before [*Gu and Wong*, 1994], support this claim.

With continuing strain, deformation in experimental shear zones becomes increasingly localized [*Marone and Kilgore*, 1993]; oblique Riedel shears become better developed and begin to dominate the gouge structure. This is often accompanied by strain weakening, demonstrating that localization represents a weaker mode of deformation [*Marone and Scholz*, 1989; *Logan et al.*, 1992; *Beeler et al.*, 1996]. At higher strains, low-angle R_1 shears extend to the shear zone boundaries, generating discontinuous boundary shears [*Marone et al.*, 1990], and the onset of stick-slip sliding [*Dieterich*, 1981; *Gu and Wong*, 1994]. Y shears, which can accommodate essentially infinite strain, dominate during this steady state phase of deformation [*Logan et al.*, 1992; *Gu and Wong*, 1994; *Beeler et al.*, 1996].

Although we have not included fracture, our simulations support the idea that deformation is more distributed for low D assemblages than for high D. Distributed deformation in our low D assemblages appears to result from frictional coupling of large particles in contact, which imparts counterrotation in particles outside a narrow zone of slip. This tends to distribute the shear load across the gouge zone, effectively widening the slip zone; a similar mechanism was proposed by *Marone et al.* [1990]. Grain bridges form, spanning the entire shear zone, and fail with continuing strain (Figure 6); the load is transferred to adjacent bridges that subsequently fail, and so on. In our simulations, the grain bridges fail by buckling, interparticle rolling, and some sliding, and the same deformation mechanisms are operative throughout the simulation. In natural fault rocks, bridges fail largely by grain fracture [e.g., *Sammis et al.*, 1987], resulting in progressive changes in PSD as well as in the dominant deformation mechanisms with strain [*Biegel et al.*, 1989; *Marone and Scholz*, 1989].

The microstructural results of the simulations corroborate field and laboratory observations that a PSD with a D value of 1.6 ($D_{3D} = 2.6$) represents a unique particle configuration associated with highly localized strain [e.g., *Sammis et al.*, 1986, 1987; *Biegel et al.*, 1989; *Marone and Scholz*, 1989]. This PSD stands out in our simulations due to the unique self organization of particles: large, isolated synthetically rolling particles in low angle slip planes are separated by columns of antithetically rolling small particles (Plate 2c). Incidentally, similar particle arrangements have also been noted in experimental gouge deformed at low normal stresses [i.e., *Morrow and Byerlee*, 1989, Figure 7; *C. Morrow*, personal communication, 1997]. As shown in Figure 8, this will tend to relieve the high frictional forces that would otherwise develop at the contacts between large rolling particles (Figure 8a); instead, frictional sliding is restricted to low force contacts between small particles outside the primary slip zone (Figure 8b). Such partitioning of deformation mechanisms may enhance strain localization at this PSD. We speculate that the preservation of this characteristic PSD in cataclastic rocks may result from the tendency for deformation in critical assemblages to localize, guiding deformation and comminution into discrete zones which undergo further comminution [e.g., *Marone and Scholz*, 1989; *Marone and Kilgore*, 1993], thereby preserving the primary PSD in the bulk of the volume.

The self-organization of particles described here is also evident in higher D simulations, suggesting that $D = 1.6$ is not a unique state but rather represents a limiting configuration containing a critical abundance of small particles that can isolate the larger particles. As discussed by *Morgan* [this issue], mechanical data from these experiments
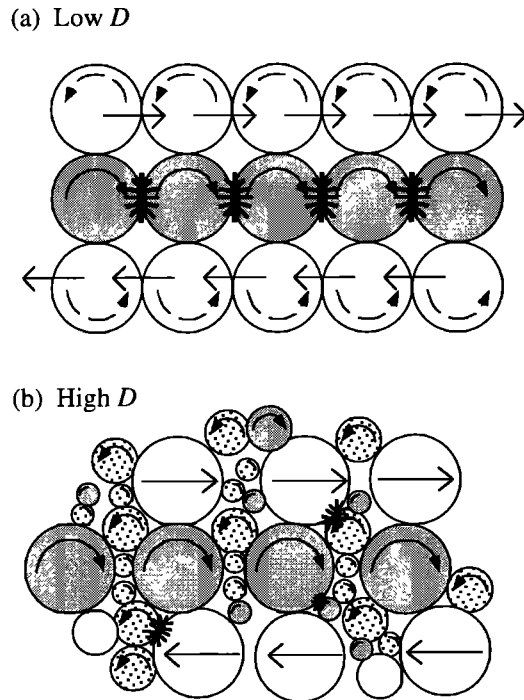
(a) Low D

(b) High D

Figure 8. Conceptual model for self-organization of rolling particles under shear for two PSD configurations. (a) Low D. Large, synthetically rolling particles (dark gray) slide against each other, experiencing high frictional resistance (black stars). The frictional resistance imparts counterrotation in adjacent particles, widening the shear zone. (b) Intermediate to high D systems. Columns of small antithetically rolling particles (stippled) form between large synthetically rolling particles, and serve as "roller bearings" that reduce frictional resistance. Sliding friction is restricted to low force contacts at the edges of the zone of slip (black stars).

support the idea that $D = 1.6$ is special, at least for the higher μ_p assemblages.

Of course, in our simulations, each assemblage begins with and maintains the same PSD configuration throughout the test. In the absence of grain fracture and distributed comminution, discrete structures develop during the initial loading phase, i.e., within the first 2% strain. Multiple, subparallel, discontinuous slip planes accommodate small amounts of slip, distributing the strain across the entire shear zone. In the higher D systems, incipient slip planes take on orientations approximately consistent with R_1, R_2, Y, or P shears. For the high μ_p experiments this initial loading phase corresponds to a period of significant shear zone dilation, which appears to be accommodated along the inclined, synthetic P shears (Plate 3c). In the low μ_p simulations, corresponding features are nearly horizontal, representing either very low angle P shears or incipient R_1 or Y shears. In laboratory experiments, discontinuous R_1 shears develop very early, denoting the first phase of localization [Logan et al., 1992; Gu and Wong, 1994], but P shears are less common, serving to link discontinuous R_1 shears into continuous, throughgoing Y shears [e.g., Mandl et al., 1977; Mandl, 1988; Logan et al., 1992]. This discrepancy in structural progression between laboratory and simulated gouges may relate to the tendency for the simulated shear zones to undergo dilation during the initial deformation as opposed to

compaction typically observed in comminuting gouge [e.g., Marone and Scholz, 1989; Morrow and Byerlee, 1989; Marone et al., 1990]. Dilation can be kinematically accommodated along P shears, while compaction would call for R_1 shears. Alternatively, the lack of P shear observations during the early stages of laboratory experiments may result from the limited number of observations of such early stages of shear deformation, especially in less common dilational systems.

At strains greater than 2-6%, anastamosing, low-angle R_1 shears in the simulations link up to produce throughgoing Y shears, which are favorably oriented to accommodate infinite displacement and therefore represent the preferred slip planes in these systems. This progression is consistent with lab observations that Y shears almost exclusively crosscut and postdate R shears [Beeler et al., 1996]. The boundary shears that others have noted [Marone et al., 1990] are inhibited in our simulations due to the roughness of the shear zone walls, but favorably smooth planes within the shear zone appear to endure for larger strain increments than others, defining persistent Y shears.

Low angle R_1 shears are observed throughout the duration of our experiments, rather than only at small strains, and give way intermittently to throughgoing Y shears. This episodic behavior relates to transient stress changes associated with shear zone loading and failure and occurs with frequencies that depend on particle abundance and mean grain size [Morgan, this issue]. Grain bridges form and fail, and particles reorganize repeatedly into new bridges that can bear similar loads as those present in the previous configuration. Similar types of microstructures occur at similar stages of each cycle. Longer-period changes in microstructure, strength, and sliding behavior, such as those observed by Beeler et al. [1996], are probably related to changes in particle size and PSD that we cannot capture here.

The R_2 shears observed throughout the simulations are unusual and unexpected features. They are abundant and well-developed but very ephemeral and occur from 2% to 200% strain. Kinematically restricted from accommodating much offset, they stand out as subtle deflections in particle displacement and zones of antithetic particle rotation. These findings suggest that R_2 shears may be equally common in natural and experimentally produced shear zones [e.g., Morrow and Byerlee, 1989; Logan et al., 1992], but in many cases they are poorly identified due to their short duration and lack of significant offset and associated particle comminution.

6.4. Effects of Grain Size and Shear Zone Thickness

Several properties and behaviors of these simulated experiments appear to scale with mean grain size. For example, the slip zones within the gouge layers tend to be about one particle wide, effectively defining a layer of roller bearings upon which the bounding gouge domains can translate. Slip zones, therefore, are much narrower for high D systems where a fine-grained matrix is present (Plate 3), than for the courser-grained low D simulations (Plate 1). The number of slip planes that can be active during a given strain interval also depends on particle abundance; the fine matrix in high D systems can accommodate multiple bands of rolling particles, whereas the abundance of slip planes in the low D systems is limited by the number of particles which span the shear zone.

These observations beg the question of whether the differences in structure observed here and the mechanical behaviors discussed by *Morgan* [this issue] may in part result from differences in mean grain size relative to shear zone thickness. There are certainly influences that may be introduced by the statistics of particle interactions. For example, laboratory experiments have demonstrated that for rough-walled shear zones, frictional strength increases as the shear zone thins [*Dieterich*, 1981; *Biegel et al.*, 1989]. This phenomenon is attributed to a decrease in the number of contacts that can fail within shortened grain bridges [*Biegel et al.*, 1989]. Frictional strength has also been observed to decrease with increase in the size of the largest particle within the power law distributed assemblage [*Biegel et al.*, 1989]. Such effects were not observed for shear zones with smooth surfaces, however, where slip may tend to be localized along the shear zone walls [*Dieterich*, 1981; *Biegel et al.*, 1989]. These factors were not formally explored in this study, although comparable behaviors and shear zone strengths were observed in representative experiments using different shear zone dimensions.

Despite the possible influences of scale on deformation behavior, certain characteristics of deformation documented in these simulations cannot be explained simply by differences in mean grain size; rather they depend on the relative abundance of particles of different sizes, arising from differences in PSD. In particular, the presence of a critical abundance of small particles interspersed among larger particles clearly influences the micromechanics of deformation in these assemblages. The organization of smaller particles into counterrotating columns cannot occur until a critical abundance of small particles is present within the assemblage, and this depends on PSD. Our observations suggest that this configuration plays a major role in defining the types and geometries of the resulting microstructures, enabling the formation of discrete R_1 and R_2 shears in the higher D systems, but less commonly in the low D systems where large particles maintain mutual frictional contacts.

7. Conclusions

The discrete numerical simulations presented here have been directed toward exploring the influence of particle size distribution (PSD) on shear zone deformation, microstructure, and localization behavior. Several of the results of this study are general and apply to all simulated assemblages; others demonstrate that PSD alone can influence deformation mode and micromechanics in granular shear zones.

1. Shear deformation in these simulations accrues through cyles of alternating distributed deformation accommodated along multiple, subhorizontal slip planes, and localized slip along discrete planes of particles. Discrete deformation structures form parallel to and oblique to the shear zone boundaries, in particular, Y shears and low- and high-angle Riedel (R_1 and R_2) shears. These show orientations similar to those observed in naturally deformed Coulomb materials. The orientations of the oblique Riedel structures are more extreme than those observed in real materials but appear to be consistent with orientations predicted for Coulomb materials with low strengths as simulated here.

2. Individual slip planes are active for up to 20% strain and subsequently are abandoned; slip is then transferred to another horizon. This results in a cumulative strain field that is

relatively homogeneous, as indicated by the linear strain markers. In the absence of PSD evolution in these assemblages, the accumulated shear strain is effectively uniform.

3. Deformation in these numerical assemblages is accommodated in large part by interparticle rolling. The distribution of rolling particles is strongly influenced by PSD and the geometry of particle packing and is strongly correlated with gouge microstructures. Low-angle R_1-shears, and horizontal Y shears are composed largely of synthetically rolling particles of various sizes, while high-angle R_2 shears are dominated by small, antithetically rolling particles. In the low D systems, large particles are in mutual contact and are frictionally coupled, leading to wide slip planes and distributed deformation. In higher D assemblages, rolling particles begin to self-organize, generating narrow rows and columns of rolling particles that may serve to enhance localization in these finer-grained assemblages by narrowing the zone of deformation. The self-organization of particles may depend on a critical abundance of small particles within the assemblage, which will isolate larger particles. Our simulations support the idea that this limiting PSD configuration is reached near $D = 1.60$, as suggested by others [e.g., *Sammis et al.*, 1986,1987; *Biegel et al.*, 1989; *Marone and Scholz*, 1989].

4. Shear loads within the granular assemblages are borne by bridges of particles carrying high average differential stresses. These bridges are inclined about 45° to the shear zone walls, parallel to the orientation of the maximum principal stress σ_1, and they evolve during shear as the shear zone is loaded and fails. Bridges fail by interparticle rolling, causing the propagation of slip planes. The extent of the grain bridge is determined by PSD; in low D assemblages a grain bridge may span the entire shear zone, whereas in higher D systems the grain bridges are very short and discontinuous.

5. Unlike natural and experimentally produced gouges in which PSD and particle shapes evolve with strain, our granular assemblages do not show clear progressions of microstructures with increasing shear strain, except during the initial loading phase of the simulations. During this phase, incipient, discontinuous shear structures develop, grow, and coalesce into throughgoing Y shears; these include incipient P shears which probably accommodate shear zone dilation during loading. Despite the lack of PSD evolution in these simulations, we gain a first peak into the micromechanisms operating in different PSD assemblages and the evolution of microstructures within complex granular systems.

Appendix

A1. General Information

The DEM program TRUBAL employs a time-stepping, finite-difference approach to solve the Newtonian equations of motion simultaneously for every particle in the system:

$$\mathbf{F}^P = m^P \, \ddot{\mathbf{x}}^P, \tag{A1}$$

$$\mathbf{M}^P = I^P \, \ddot{\theta}^P, \tag{A2}$$

where $\mathbf{F}^P$ and $\mathbf{M}^P$ are the net force and moments acting on a given particle, m^P and I^P are the mass and moment of inertia, and $\ddot{\mathbf{x}}^P$ and $\ddot{\theta}^P$ are the linear and angular accelerations of the particles, respectively. In a typical calculation cycle (Figure A1), known velocities of the particles are used to compute
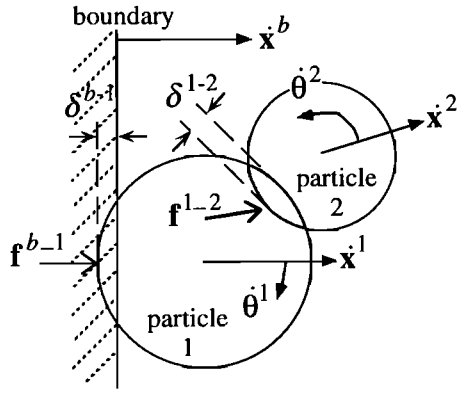
Figure A1. Schematic diagram of particle interactions in DEM. Lateral velocity of the boundary $\dot{x}^b$ cause displacement and overlap with particle 1 by δ^{b-1} imparting a force f^{b-1} and acceleration of particle 1. The resolved velocity $\dot{x}^1$ and subsequent displacement of particle 1 causes overlap with particle 2 by δ^{1-2}, imparting a contact force f^{1-2} with both normal and shear components. The resultant force causes both linear and angular accelerations on both particles, which are integrated to determine instantaneous velocities $\dot{x}^1$, $\dot{x}^2$, $\dot{\theta}^1$, and $\dot{\theta}^2$. If the contact shear stress is high enough, sliding can also occur.

relative velocities at interparticle contacts, which are integrated to obtain the relative displacements at the contacts. Employing suitable contact laws, the instantaneous values of interparticle contact forces are determined and summed to obtain the net force and moment on the particle. These are then plugged into equations (A1) and (A2) to calculate new particle displacements and rotations. Particle motions are induced by gravitational forces, by external forces prescribed by stress or strain rate boundary conditions, and by forces resolved at interparticle contacts. Strain rates are assumed to be low, and small time steps Δt are chosen to ensure that the disturbance of a given particle only propagates to its immediate neighbors, and inertial forces within the quasi-static system remain small [*Cundall*,1971; *Haff*, 1993]. Particle displacements are unrestricted, so the system can accumulate very large strains, a difficult feat using continuum numerical methods [e.g., *Willet*, 1992; *Fullsack*, 1995].

A2.   Contact Laws

The net force and moment on each particle depends on the choice of interparticle contact laws. Cohesionless, granular materials are commonly assumed to be composed of elastic-frictional particles which obey Hertz-Mindlin contact theory [e.g., *Johnson*, 1985]. Particles respond elastically to normal forces at their boundaries, leading to nonlinear repulsions scaled to the contact areas; for the spheres modeled by TRUBAL, the components of the normal force are given by

$$f^a{}_{(n)_i} = \frac{4\sqrt{RG}}{3(1-v)}\delta_i^{3/2},   \qquad (A3)$$

where the effective radius R is defined such that $1/R = 1/R_1 + 1/R_2$, G is the bulk modulus, v is Poisson's ratio, and δ_i gives the ith component ($i = 1,2,3$) of the particle interpenetration (or elastic deformation if the simulated particles could deform). The components of the shear force resolved at the contact are given by

$$f^a{}_{(s)_i} = (f^a{}_{(n)})^{1/3}\frac{(4G)^{2/3}(3R(1-v))^{1/3}}{(2-v)}\delta_t,   \qquad (A4)$$

where $f^a{}_{(n)}$ represents the magnitude of the normal force. If the magnitude of the shear force $f^a{}_{(s)}$ exceeds the critical shear force given by the Coulomb criterion for frictional sliding

$$f^a{}_{(s)_{max}} = S_0 + \mu_c f^a{}_{(n)},   \qquad (A5)$$

where S_0 and μ_c are interparticle cohesion and contact friction respectively, then slip occurs and the shear force is scaled back to $f^a{}_{(s)_{max}}$. For the noncohesive particles used here, $S_0 = 0$.

The net force and moment on a given particle is given by the sum of the contributions from all of the contacts on that particle n_c^p (Figure A1),

$$F_i^p = \sum_{a=1}^{n_c^p}(f^a{}_{(n)_i} + f^a{}_{(s)_i}),   \qquad (A6)$$

$$M_i^p = \sum_{a=1}^{n_c^p}(\varepsilon_{ijk}f^a{}_{(s)_j}\, r_k^a),   \qquad (A7)$$

where ε_{ijk} is the alternation tensor and r_k^a are the components of the particle radius normal to contact a (summation is assumed on repeated indices). These give the quantities which must be substituted back into the equations of motion to calculate particle velocities and displacements. In this constrained system, gravitational forces have been neglected.

A3.   Equations of Motion and Properties of the Assemblage

The numerical solution of equations (A1) and (A2) is obtained by integration, assuming constant velocities and accelerations for a given time step (Figure A1). An explicit, central difference, time-stepping scheme is used [*Cundall and Strack*, 1979]; velocities (given in components) are determined in the middle of each time step,

$$(\dot{x}_i)_{n+\frac{1}{2}} = (\dot{x}_i)_{n-\frac{1}{2}} + (F_i^p)_n\frac{\Delta t}{m^p},   \qquad (A8)$$

$$(\dot{\theta}_i)_{n+\frac{1}{2}} = (\dot{\theta}_i)_{n-\frac{1}{2}} + (M_i^p)_n\frac{\Delta t}{I^p},   \qquad (A9)$$

and particle displacements and rotations at the next time step are calculated from the average velocities:

$$(x_i)_{n+1} = (x_i)_n + (\dot{x}_i)_{n+\frac{1}{2}}\Delta t,   \qquad (A10)$$

$$(\theta_i)_{n+1} = (\theta_i)_n + (\dot{\theta}_i)_{n+\frac{1}{2}}\Delta t,   \qquad (A11)$$

Damping of particle motions must be included in the calculations to prevent the continuous oscillation of an elastic system. Numerically, this depends on an arbitrary parameter that guarantees that the system can reach a steady state; physically, damping can arise from loss of energy in the system by heat generation and inelastic deformation of the particles. Several damping methods are possible [e.g., *Cundall*, 1987]; here, viscous damping is provided at interparticle contacts by introducing terms which scale the velocities in equation (A9). A more complete discussion is

given elsewhere [*Cundall and Strack*, 1979; *Cundall*, 1987; *Walton*, 1995].

Cundall and Strack [1983] and *Thornton and Barnes* [1986] have shown that the average stress of a particle can be calculated by summing the tractions due to discrete contact forces at the particle surface

$$\sigma_{ij}^P = \frac{1}{V^P} \sum_{a=1}^{n_c^P} (r_i^a f_j^a), \tag{A12}$$

where V^P is the volume of the particle, and $f_i^a = f^a{}_{(n)_i} + f^a{}_{(s)_i}$ is the total force acting in the ith direction at contact a. This leads to consistent particle stresses for a given proportional particle overlap, δ/R, independent of particle volume V^P. The average stress in a region of the assemblage comes from summing the average particle stresses over the particles within that region N_p, leading to the relationship

$$\overline{\sigma}_{ij} = \frac{1}{V} \sum_{p=1}^{N_p} \sum_{a=1}^{n_c^P} (r_i^a f_j^a), \tag{A13}$$

where V is the volume of the averaging domain. In this way, principal stress orientations can be plotted throughout the domain, yielding the spatial stress field. If desired, the stress tensor can be decomposed into normal and shear components which contribute to the fabric of the assemblage [*Cundall and Strack*, 1983; *Cundall*, 1987].

In order to obtain a measure consistent with quantities measured in the laboratory, the shear stress τ and normal stress σ_n acting on the shear zone walls are calculated by summing the tangential and normal forces acting on the walls (e.g., on the particles comprising the walls), respectively:

$$\tau = \frac{1}{2} \left[\sum_w \sum_p (-1)^w F_1^p \right], \tag{A14}$$

$$\sigma_n = \frac{1}{2} \left[\sum_w \sum_p (-1)^w F_2^p \right], \tag{A15}$$

where F_i^p is the net force acting on a particle in the ith direction and w represents the wall ($w = 1,2$). The factor of -1 raised to the power of w accounts for the fact that the forces contributing to the tractions on the walls act in the opposite directions.

References

Allen, M.P., and D.J. Tildesley, *Computer Simulations of Liquids*, Clarendon, Oxford, England, 1987.

Antonellini, M.A., and D.D. Pollard, Distinct element modeling of deformation bands in sandstone, *J. Struct. Geol., 17*, 1165-1182, 1995.

Beeler, N.M., T.E. Tullis, M.L. Blanpied, and J.D. Weeks, Frictional behavior of large displacement experimental faults, *J. Geophys. Res., 101*, 8697-8715, 1996.

Biegel, R.L., C.S Sammis, and J.H. Dieterich, The frictional properties of a simulated gouge having a fractal particle distribution, *J. Struct. Geol., 11*, 827-846, 1989.

Blenkinsop, T G., Cataclasis and processes of particle size reduction, *Pure Appl. Geophys., 136*, 59-86, 1991.

Bruno, M.S., and R.B. Nelson, Microstructural analysis of inelastic behavior of sedimentary rock, *Mech. Mater., 12*, 95-118, 1991.

Byerlee, J.D., Friction of rocks, *Pure Appl. Geophys., 116*, 615-626, 1978

Chester, F.M., and J.M. Logan, Composite planar fabric of gouge from the Punchbowl Fault, California, *J. Struct. Geol., 9*, 621-634, 1989.

Cladouhos, T.T , Shape preferred orientations of survivor grains in fault gouge, *J. Struct. Geol.*, in press, 1998.

Cundall, P.A., A computer model for simulating progressive, large - scale movements in blocky rock systems, *Proc Symp. Int. Soc. Rock Mech., Nancy* 2, 1971.

Cundall, P.A., Distinct element models for rock and soil structure, in *Analytical and Computational Methods in Engineering Rock Mechanics*, edited by E.T. Brown, pp. 129-163, Allen and Unwin, London, 1987.

Cundall, P.A., Computer simulations of dense sphere assemblies, in *Micromechanics of Granular Materials*, edited by M Satake and J.T. Jenkins, pp. 343-352, Elsevier Sci., New York, 1988.

Cundall, P.A., and R.D. Hart, Numerical modeling of discontinua, in *Proceedings, 1st U.S. Conference on Discrete Element Methods*, edited by G.G.W. Mustoe, M. Henriksen, and H.-P. Huttelmaier, CSM Press, Golden, Colo , 1989.

Cundall, P A., and O.D.L. Strack, A discrete numerical model for granular assemblies, *Geotechnique, 29*, 47-65, 1979.

Cundall, P.A., and O.D.L. Strack, Modeling of microscopic mechanisms in granular material, in *Mechanics of Granular Materials: New Models and Constitutive Relations*, edited by J.T. Jenkins and M. Satake, pp. 137-149, Elsevier Sci., New York, 1983.

Cundall, P.A., A. Drescher, and O.D.L. Strack, Numerical experiments on granular assemblies: Measurements and observations, in *Deformation and Failure of Granular Materials*, edited by P.A. Vermeer and H.J. Luger, pp. 355-370, A.A. Balkema, Brookfield, Vt., 1982.

Dieterich, J.H., Constitutive properties of faults with simulated gouge, in *Mechanical Behavior of Crustal Rocks, Geophys. Monogr Ser.*, vol. 24, edited by N.L. Carter et al., pp. 108-120, AGU, Washington, D.C., 1981.

Evans, J.P., and F M. Chester, Fluid-rock interaction in faults of the San Andreas system: Inferences from San Gabriel fault rock geochemistry and microstructures, *J. Geophys. Res., 100*, 13,007-13,020, 1995.

Feda, J., *Mechanics of Particulate Materials: The Principles*, Elsevier Sci., New York, 1982.

Fullsack, P., An arbitrary Lagrangian-Eulerian formulation for creeping flows and its application in tectonic models, *Geophys. J. Int., 120*, 1-23, 1995.

Gu, Y., and T.-F. Wong, Development of shear localization in simulated quartz gouge: Effects of cumulative slip and gouge particle size, *Pure Appl. Geophys., 143*, 387-423, 1994.

Haff, P., Discrete mechanics, in *Granular Matter: An Interdisciplinary Approach*, edited by A. Mehta, pp. 141-160, Springer-Verlag, New York, 1993.

Hooke, R.L., and N.R. Iverson, Grain-size distribution in deforming subglacial tills: Role of fracture, *Geology, 23*, 57-60, 1995

Johnson, K.L , *Contact Mechanics*, Cambridge Univ Press, New York, 1985.

Logan, J.M., M. Friedman, N.G. Higgs, C. Dengo, and T. Shimamoto, Experimental studies of simulated gouge and their application to studies of natural fault zones, in *Proceedings of Conference VIII, Analysis of Actual Fault Zones in Bedrock, U.S. Geol. Surv., Open File Rep., 79-1239,* 305-343, 1979.

Logan, J.M., C.A. Dengo, N G. Higgs, and Z.Z. Wang, Fabrics of experimental fault zones: Their development and relationship to mechanical behavior, in *Fault Mechanics and Transport Properties in Rocks,* edited by B. Evans and T.-F. Wong, pp. 33-67, Academic Press, New York, 1992.

Malan, D.F., and J.A.L. Napier, Computer modelling of granular material microfracturing, *Tectonophysics, 248,* 21-37, 1995

Mandl, G., *Mechanics of Tectonic Faulting,* Elsevier Sci., New York, 1988.

Mandl, G., L.N J de Jong, and A. Maltha, Shear zones in granular material, *Rock Mech., 9,* 95-144, 1977

Marone, C., and B. Kilgore, Scaling of the critical slip distance for seismic faulting with shear strain in fault zones, *Nature, 362,* 618-621, 1993.

Marone, C, and C.H. Scholz, Particle size distribution and microstructure within simulated fault gouge, *J. Struct. Geol., 11,* 799-814, 1989.

Marone, C., C.B. Raleigh, and C H. Scholz, Frictional behavior and constitutive modeling of simulated fault gouge, *J. Geophys. Res., 95,* 7007-7025, 1990.

Morgan, J.K., Numerical simulations of granular shear zones using the distinct element method, 2. Effects of particle size distribution and interparticle friction on mechanical behavior, *J. Geophys. Res.,* this issue

Morgan, J.K., T.T. Cladouhos, K.M. Scharer, D.S. Cowan, and P. Vrolijk, Fractal particle size distributions in Death Valley fault zones: Controls on mechanics and kinematics of fault rocks, *Eos Trans. AGU, 77(46),* Fall Meet Suppl., F717, 1996.

Morrow, C.A., and J.D. Byerlee, Experimental studies of compaction and dilatancy during frictional sliding on faults containing gouge, *J. Struct. Geol., 11,* 815-825, 1989

Nasuno, S., A. Kudrolli, and J.P Gollub, Friction in granular laters: Hysteresis and Precursors, *Phys. Rev., Lett., 79,* 949-951, 1997

Riedel, W., Zur Mechanik geologischer Brucherscheinungen, *Centralbl. Mineral. Abt. B,* 354-368, 1929.

Robertson, E C., Continuous formation of gouge and breccia during fault displacement, in *Issues in Rock Mechanics,* edited by R.E. Goodman and F. Hulse, *Proc. Symp. Rock Mech., 23rd,* 397-404, 1982.

Sadd, M.H., and J.Y. Gao, The effect of particle damage on wave propagation in granular materials, in *Mechanics of Deformation and Flow of Particulate Materials,* 159-173, Am. Soc. of Civ Eng., New York, 1997.

Sammis, C., and R. L. Biegel, Fractals, fault-gouge, and friction, *Pure Appl. Geophys, 131,* 256-271, 1989.

Sammis, C., and S.J. Steacy, The micromechanics of friction in a granular layer, *Pure Appl. Geophys., 142,* 777-794, 1994.

Sammis, C.G., R.H. Osborne, J.L. Anderson, M. Banerdt, and P. White, Self-similar cataclasis in the formation of fault gouge, *Pure Appl. Geophys., 124,* 53-78, 1986.

Sammis, C., G. King, and R. Biegel, The kinematics of gouge deformation, *Pure Appl. Geophys., 125,* 777-812, 1987.

Scholz, C.H., Wear and gouge formation in brittle faulting, *Geology, 15,* 493-5, 1987.

Scholz, C.H , *The Mechanics of Earthquakes and Faulting,* Cambridge Univ. Press, New York, 1990.

Scott, D.R , Seismicity and stress rotation in a granular model of the brittle crust, *Nature, 381,* 592-595, 1996.

Thornton, C , and D J. Barnes, Computer simulated deformation of compact granular assemblies, *Acta Mech., 64,* 45-61, 1986.

Trent, B.C., and L.G. Margolin, Modeling fracture in cemented granular materials, in *Fracture Mechanics Applied to Geotechnical Engineering,* edited by L.E. Vallejo and R.Y Liang, *ASCE Geotech. Spec. Pub.* 43, pp. 54-69, Am. Soc. of Civ. Eng., New York, 1994.

Trent, B.C., and L.G. Margolin, Numerical validation of a constitutive theory for an arbitrarily fractured solid, *Eng Comput., 12,* 125-134, 1995

Turcotte, D.L , Fractals and fragmentation, *J Geophys. Res., 91,* 1921-1926, 1986.

Walton, O.R., Force models for particle-dynamics simulations of granular materials, in *Mobile Particulate Systems,* edited by E. Guazzelli and L. Oger, pp. 366-378, Kluwer Acad., Norwell, Mass.,1995.

Wessel, P , and W.H.F. Smith, The generic mapping tools (GMT), version 3.0, Technical Reference & Cookbook, Sch. of Ocean and Earth Sci. and Technol , Honolulu, Hawaii, 1995.

Willet, S.D , Dynamic and kinematic growth and change of a Coulomb wedge, in *Thrust Mechanics,* edited by K.R. McClay, pp. 19-32, Chapman and Hall, New York, 1992.

Williams, J.K., and N. Rege, Coherent vortex structures in deforming granular materials, *Mech. Cohesive Frictional Mater., 2,* 223-236, 1996.

Wong, T.-F , C. David, and W Zhu, The transition from brittle faulting to cataclastic flow in porous sandstones: Mechanical deformation, *J. Geophys. Res., 102,* 3009-3025, 1997.

Wood, D.M., *Soil Behavior and Critical State Soil Mechanics,* Cambridge Univ Press, New York, 1990.

Zhang, J., T.-F. Wong, and D.M. Davis, Micromechanics of pressure induced grain crushing in porous rocks, *J. Geophys Res, 85,* 341-352, 1990.

M.S. Boettcher, Department of Geological Sciences, Brown University, Providence, RI 02912.

J.K. Morgan, Department of Geology and Geophysics, SOEST, University of Hawaii, 2525 Correa Road, Honolulu, HI 96822. (morgan@soest.hawaii edu)